# Hemispherical imaging of skin with polarized light

Jessica C. Ramella-Roman,[a,b] Bruno Boulbry,[b] and Thomas A. Germer[b]

[a]Department of Biomedical Engineering, The Catholic University of America, Washington, DC 20064
[b]Optical Technology Division, National Institute of Standards and Technology, Gaithersburg, MD 20899

## ABSTRACT

Polarized light imaging has been used in the past for skin-cancer edge detection from skin lesions. In the standard imaging modality, the source, detector, and sample are usually aligned in the same plane, and the effect of the air-skin boundary is minimized using a glass slide with an index matching fluid. In this study, we investigate polarized light imaging of skin surfaces using a novel instrument that enables out-of-plane illumination. Stokes vector images are acquired for any one of sixteen different illumination directions and used to study the effect of skin roughness as well as surface and subsurface scattering. We show that the effect of skin roughness can be minimized or enhanced, depending upon the incident direction and polarization. In the former case, the need for a glass slide with an index matching fluid can be reduced. In the latter, surface topography can be more clearly discerned.

**Keywords:** Scattering, polarimetry, skin

## 1. INTRODUCTION

Polarized light has been used in the past to enhance contrast in images of superficial skin features [1,2]. Figure 1 shows a simple layout for such measurements. Polarizers are used in both the illumination and the imaging path. Typically [1] two images are acquired: one where the polarizers are aligned with respect to each other, and the second where they are crossed. A composite image, formed from the difference between these two images, highlights features which preserve the original polarization state. A glass slide and an index-matching fluid are used to minimize the effect of skin roughness and to increase the sensitivity of the measurement to subsurface features.

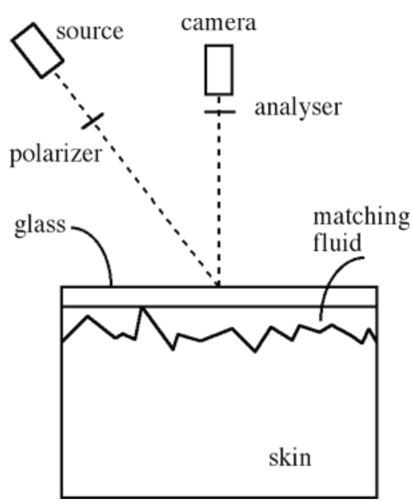


**Figure 1.** A simple polarized light imaging layout

Studies on rough surface scattering [3] conducted at the National Institute of Standards and Technology (NIST) on non-biological samples have shown that polarized light can be used to discriminate different scattering mechanisms. The rough surface scattering component can often be eliminated by changing the direction of the source and choosing the polarization of the illumination and collection wisely. Figure 2 shows the geometry for out-of-plane measurements, where $\theta_i$ is the incident polar angle, $\theta_s$ is the scattering polar angle, and $\phi_s$ is the azimuth, or out-of-plane, angle.

Saratov Fall Meeting 2006: Optical Technologies in Biophysics and Medicine VIII, edited by
Valery V. Tuchin, Proc. of SPIE Vol. 6535, 65350U, (2007) · 1605-7422/07/$18 · doi: 10.1117/12.740962

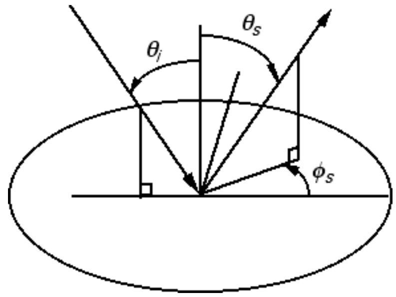

**Figure 2.** Out of plane geometry

For a given scattering geometry, we measure the Stokes vector intensity **S** of the back-reflected light, modulating the detector polarizing elements. The Stokes vector can be divided into its polarized and unpolarized components

$$\mathbf{S} = \begin{bmatrix} S_o & S_1 & S_2 & S_3 \end{bmatrix}^{\mathrm{T}} = I_{\mathrm{unpol}} \begin{bmatrix} 1 & 0 & 0 & 0 \end{bmatrix}^{\mathrm{T}} + I_{\mathrm{pol}} \begin{bmatrix} 1 & S_1/S_{\mathrm{pol}} & S_2/S_{\mathrm{pol}} & S_3/S_{\mathrm{pol}} \end{bmatrix}^{\mathrm{T}}$$

where

$$S_{\mathrm{pol}} = \left(S_1^2 + S_2^2 + S_3^2\right)^{1/2} .$$

We also characterize the polarization in terms of the principle angle of the polarization ellipse,

$$\eta = \arctan(S_2 / S_1) / 2 ,$$

and by the degree of circular polarization,

$$P_{\mathrm{C}} = S_3 / S_0 .$$

## 2. MODELING

Skin is a very complex layered media exhibiting multiple scattering components. In order to simulate such complexity we use a combination of mechanisms, such as rough surface scattering from the stratum corneum and dermoepidermal junction, single scattering from cell nuclei, and multiple scattering from cells and collagen bundles. Rough surface scattering can be approximated with a simple facet model [5], where light rays are assumed to reflect specularly from a distribution of surface facets, or a micro-roughness model [6], which is a diffractive model based upon first-order vector perturbation theory. Subsurface scattering can be modeled as a sum of a single scattering component, based upon a Henyey-Greenstein phase function beneath a smooth interface, and a diffuse multiple scattering component beneath a smooth interface [7]. Both subsurface models include the effects of transmission through the smooth exposed interface. Although these models are very simple and cannot capture the full complexity of the skin individually, their combination is showing promising results. For example, we will show that the rough surface can be modeled both with a facet model (for large scale roughness such as wrinkles and glyph lines), as well as with a microroughness model (for roughness with amplitude much less than the wavelength of the light, such as from cells in the stratum corneum).

In our analysis, we use models included in the Modeled Integrated Scatter Tool (MIST) [8]. The MIST program, based upon the SCATMECH library of scattering codes [9], was developed to model an integrated scattering system, but can also be used to evaluate the intensity and polarization of light scattered in specific geometries and to study their dependence on model parameters.

## 3. MATERIAL AND METHODS

Figure 3 shows a new experimental layout with no moving parts that was built in order to acquire Stokes vector images as functions of illumination direction. The system consists of sixteen illumination tubes directed towards a sample position. Each illumination tube, shown schematically in Fig. 4, has a tri-color light emitting diode (LED), a dichroic sheet polarizer, and a lens and provides collimated and linearly polarized light centered at wavelengths 472 nm, 525 nm, and 633 nm. Each polarizer is aligned so that the incident illumination is linearly polarized with its electric field 45° from the plane of incidence (in some previous work, we used a 90° polarization, or the electric field in the plane of incidence [10]). One illuminator has a polar angle of $\theta_i = 0°$, six have a polar angle $\theta_i = 24°$, and nine have a polar angle $\theta_i = 49°$.

A 12-bit digital charge-coupled device (CCD) views the sample with a polar angle of $\theta_s = 49°$. Two liquid crystals variable retarders (LC1 and LC2) followed by a polarizer (POL) modulate the scattered light before reaching the camera. The rotation of the retarders and the polarizer remain fixed, while the retardances are chosen to span the Poincarré sphere and enable Stokes vector measurements.

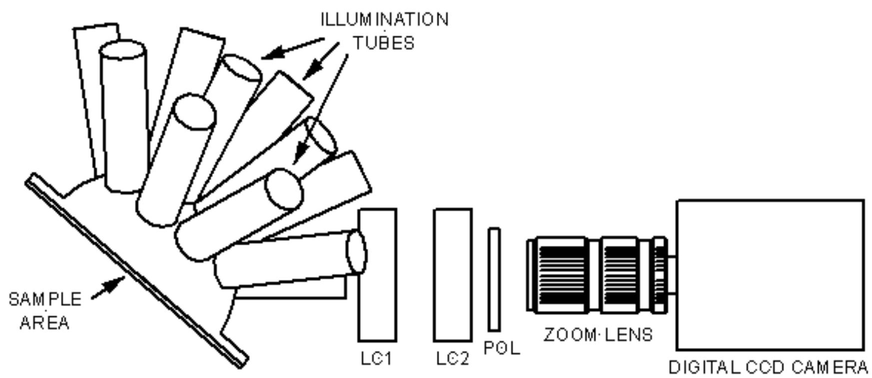


**Figure 3.** Schematic diagram of the hemispherical illumination system and the imaging polarimeter.

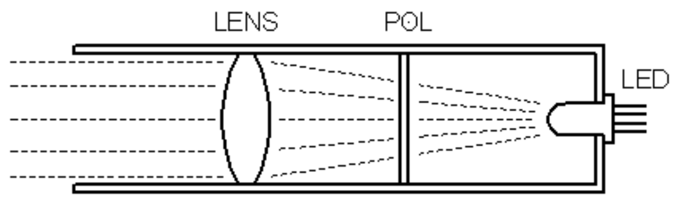


**Figure 4.** Schematic diagram of an illumination tube.

The system was calibrated with a rough gold standard. Figure 5 shows results for how $\eta$ varies with $\phi_s$. The dominant mechanism of scattering from the gold standard is rough surface scattering. A facet model (curves in Fig. 5) is able to describe the modulation of $\eta$ very well. The complex index of refraction for gold used in the model was 1.29+1.81i at 472 nm, 0.53+2.28i at 525 nm, and 0.18+3.7i at 633 nm, respectively.

## 4. RESULTS

Experiments were conducted on freshly excised porcine skin samples. A portion of the skin sample was smeared with index-matching gel and covered with a thin glass slide, as illustrated in Fig. 6. The covered portion allowed for a quick elimination of the rough surface effect in one section of the image. The remaining part of the skin sample was left untouched; rough surface scattering effects were most visible in this section.

Figures 7 and 8 show results for the glass-slide-covered portion of the skin sample for two different incident angles $\theta_i$. The graphs show the $\phi_s$ dependent variation of the principal angle of polarization $\eta$ for $\theta_i$=24° (Fig. 7) and $\theta_i$=49° (Fig. 8). The error bars in all plots represent the standard deviation of the mean of the data. A two-sources subsurface model, obtained by summing the single scattering and diffuse scattering models described above, was used to model the data shown in Figs. 7 and 8. We used an anisotropy factor $g = 0.98$, a scattering coefficient $\mu_s$= 600 cm$^{-1}$, and a diffuse reflectance of 0.05 to model the data; these values are close to, but not identical, to those found elsewhere in the literature [7].

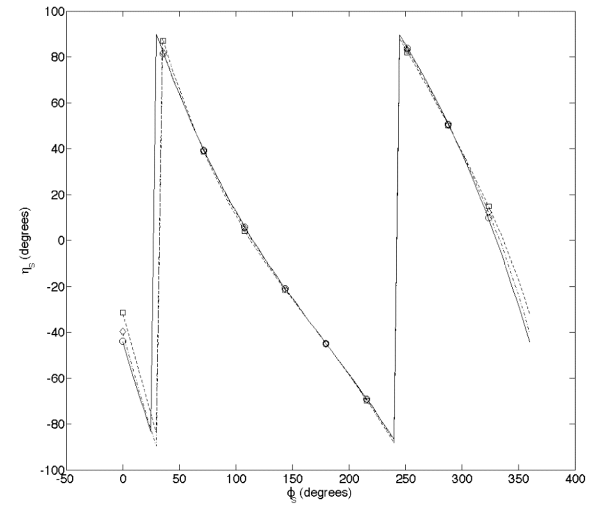


**Figure 5.** The average principal angle of the polarization measured from a rough gold standard illuminated at $\theta_i$ =49°. The symbols are the experimental results, and the curves represent the facet scattering model: (circles, solid curve) 633 nm, (diamonds, dash-dotted curve) 525 nm, and (squares, dashed curve) 472 nm. Error bars corresponding to the standard deviation of the mean are smaller than the symbols.

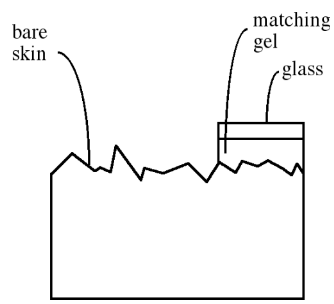


**Figure 6.** Portions of the porcine skin samples were covered with a glass slide and matching gel.

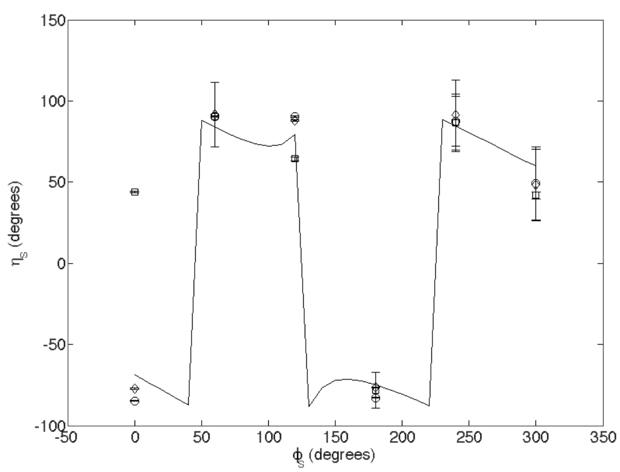

**Figure 7.** Principle angle of polarization measured for a glass-slide-covered skin sample for $\theta_i$=24°. The symbols are for (circles) 633 nm, (diamonds) 525 nm, and (square) 472 nm. The curves represent the predictions of the subsurface model described in the text.

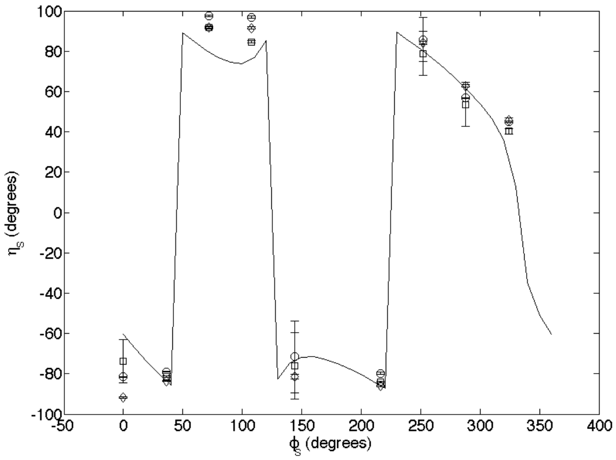


**Figure 8.** Principle angle of polarization measured for a glass-slide-covered skin sample for $\theta_i$=49°. The symbols are for (circles) 633 nm, (diamonds) 525 nm, and (square) 472 nm. The curves represent the predictions of the subsurface model described in the text.

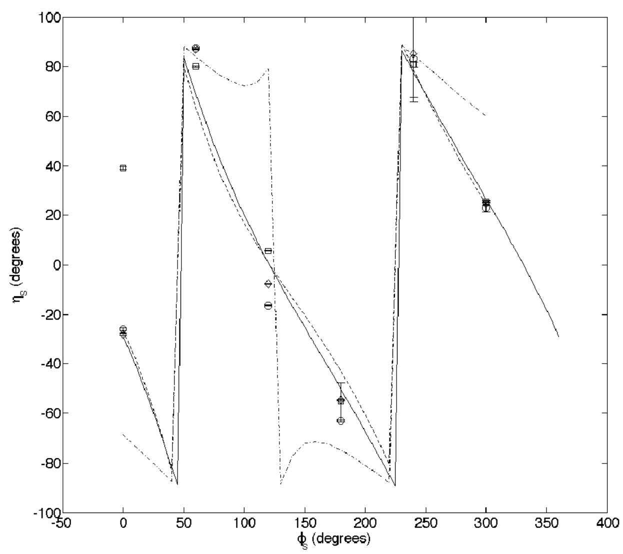


**Figure 9.** Principle angle of polarization measured for an uncovered skin sample for $\theta_i$=24°. The symbols are for (circles) 633 nm, (diamonds) 525 nm, and (square) 472 nm. The dash-dot line corresponds to the two sources model. The solid line is the microrough model and the dashed line is the facet model.

It is interesting to notice how a simple combination of single and multiple scattering mechanisms is able to capture the data trend for both $\theta_i$=24° and $\theta_i$=49°. In contrast, Figs. 9 ($\theta_i$=24°) and 10 ($\theta_i$=49°) show the results obtained from the skin sample where the rough surface is not covered by the glass slide. The results shown in Figs. 9 and 10 do not follow those of the subsurface model. For $\theta_i$=24°, the data can be modeled with a simple facet model (dashed curve) or with a microroughness model (solid curve). The most appropriate model would most likely be a combination of a roughness model with the combination subsurface model. However, there are too many parameters to adjust to guarantee a unique solution.

While the roughness models work fairly well alone for $\theta_i$=24°, the roughness models fail to match the data for $\theta_i$=49°. The subsurface scattering may be contributing substantially at this angle. The dashed line corresponds to the combination subsurface model used for the matched data and the solid line corresponds to the microroughness model.

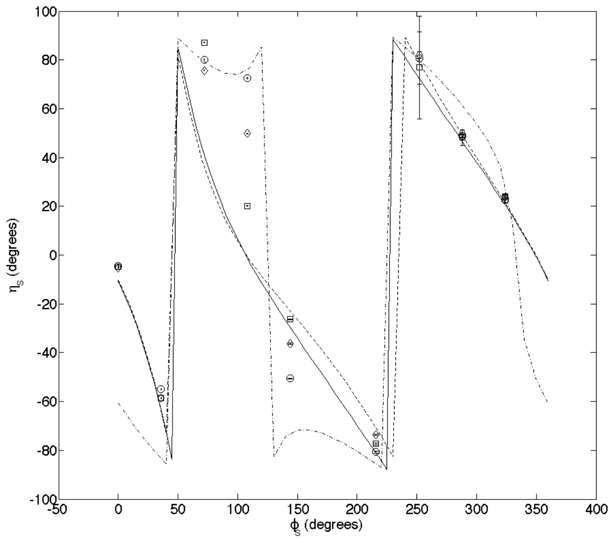


**Figure 10.** Principle angle of polarization measured for an uncovered skin sample for $\theta_i$=49°. The symbols are for (circles) 633 nm, (diamonds) 525 nm, and (square) 472 nm. The dash-dot line corresponds to the two sources model. The solid line is the microrough model and the dashed line is the facet model.

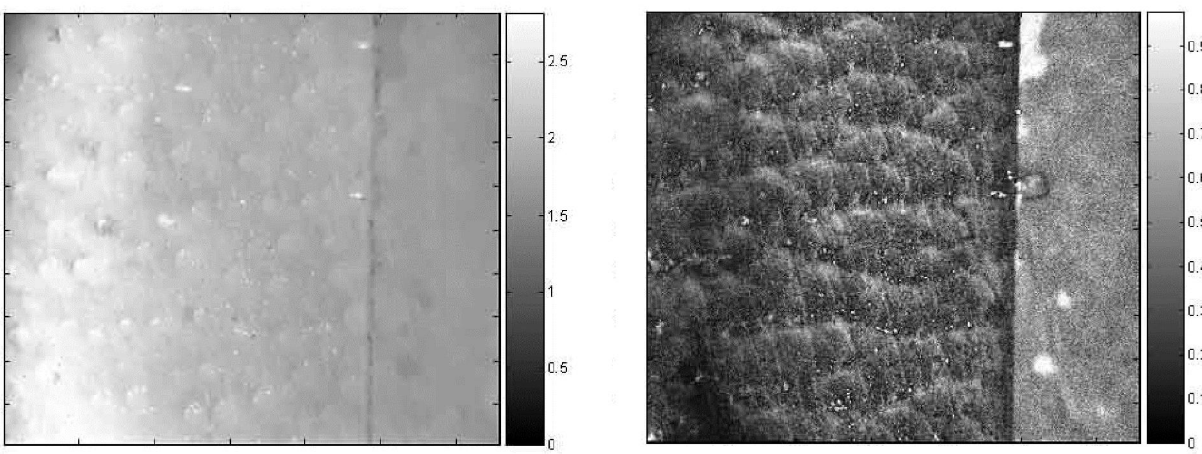


**Figure 11.** $S_0$ (left) for images obtained using 633 nm illumination for $\theta_i$ = 49° and $\phi_s$ =114° and (right) the corresponding $S_{pol}$ image. The image area was about 1.5 cm$^2$.

Measurements conducted with the blue wavelength (472 nm) tend to behave closer to the predictions of the facet model for both small and large $\theta_i$ angles, possibly indicating shallower penetration and a concomitant decrease in subsurface scatter. While for green (525 nm) and especially for red (633 nm) illumination and $\theta_i$ =49°, the data diverges from the facet model and tends towards the combination surface model. In our experiments azimuth angles between 50° and 180° seem to be particularly sensitive to tissue orientation and anisotropy.
Images obtained at $\theta_i$=24° and $\phi_s$=114°, where the data deviated the most from the facet model are shown in Fig. 11. On the left hand side we show the intensity image $S_0$, and on the right hand side we show the corresponding $S_{pol}$ images.

Figures 12 shows the data collected with 633 nm illumination at $\theta_i$ = 24° and $\phi_s$ = 0°, where the results are described well by the facet model. The images obtained at these angles are very different from the ones shown in Fig. 11. Rough surface scattering is a dominant mechanism at these angles.

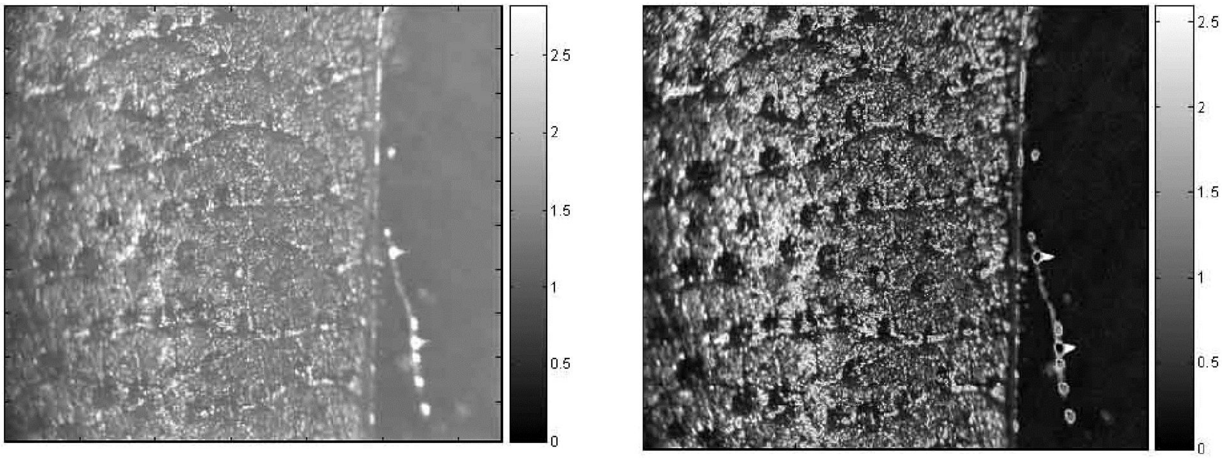


**Figure 12.** $S_0$ (left) for images obtained using 633 nm illumination for $\theta_i$ = 24° and $\phi_s$ =0°, and (right) the corresponding $S_{pol}$ image. The image area was about 1.5 cm$^2$.

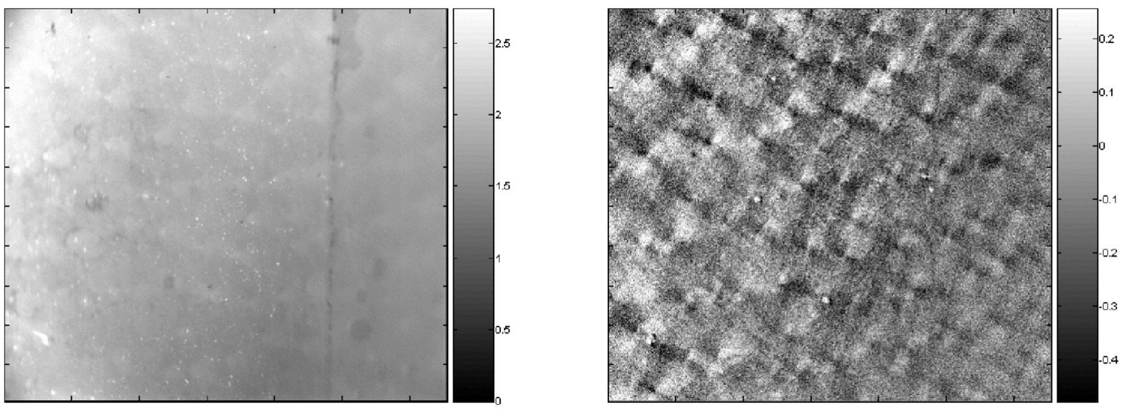


**Figure 13.** $S_0$ (left) for images obtained using 633 nm illumination for $\theta_i$ = 49° and $\phi_s$ =216°, and (right) the corresponding $P_c$ image. The image area was about 1.5 cm$^2$.

Finally, in Fig. 13, we show images of the degree of circular polarization obtained at $\theta_i$ = 49° and $\phi_s$ = 216°. For this illumination direction, the effect of the rough surface is nearly eliminated. That is, no real difference is visible between the covered and the uncovered sections of the image. The presence of circular polarization is not understood at this time.

## 5. CONCLUSIONS

We have studied polarized light scattering from skin surfaces. The effect of rough surface scattering follows a rough surface model at a shallow incident angle $\theta_i$ = 24°. At a larger incident angle $\theta_i$ = 49°, other effects such as sub-surface scattering play a role. Images of the polarized part of the back-reflected beam show different features for equal $\theta_i$ and different azimuth angles $\phi_s$. Images of the degree of circular polarization captured at angle $\theta_i$ = $\theta_s$ =49° and $\phi_s$ =216° seemed insensitive to surface roughness and produced almost identical results when images with and without a matched boundary.

## REFERENCES


1. S. L. Jacques, J.C. Ramella-Roman, and K. Lee, "Imaging Superficial Tissues with Polarized Light," Lasers Surg. Med. **26**, 119–129 (2000).
2. S.L. Jacques, J.C. Ramella-Roman, and K. Lee, "Imaging skin pathology with polarized light," J. of Biomedical Optics **7**, 329–340 (2002).
3. T.A. Germer, "Polarized light scattering by microroughness and small defects in dielectric layers," J. Opt. Soc. Am. A **18**, 1279–1288 (2001).
4. B. Boulbry, J.C. Ramella-Roman, and T. A. Germer, "A novel hemispherical spectro-polarimetric scattering instrument for skin lesion imaging," in *Photonic Therapeutics and Diagnostics II*, N. Kollias, *et al.*, Eds., Proc. SPIE **6078**, 128–134 (2006).
5. K.E. Torrance and E.M. Sparrow, "Theory of off-specular reflections from roughened surfaces," J. Opt. Soc. Am. **57**, 1105–1114 (1967).
6. Jun Q. Lu, Xin-Hua Hu, and Ke Dong, "Modeling of the rough-interface effect on a converging light beam propagating in a skin tissue phantom," Appl. Opt. **39**, 5890–5897 (2000).
7. S. L. Jacques, C. A. Alter, and S. A. Prahl, "Angular Dependence of HeNe Laser Light Scattering by Human Dermis," Lasers Life Sci. **1**, 309–333 (1987).
8. Modeled Integrated Scatter Tool (MIST), available from http://physics.nist.gov/scatmech.
9. SCATMECH: Polarized Light Scattering C++ Library, available from http://physics.nist.gov/scatmech.
10. J.C. Ramella-Roman, D. Duncan, T. A. Germer, "Out-of-plane polarimetric imaging of skin: Surface and subsurface effects," in *Photonic Therapeutics and Diagnostics*, K.E. Bartels, *et al.*, Eds., Proc. SPIE **5686**, 142-153 (2005).